

# Minimal Altitude Loss Pullout Maneuvers

Roberto A. Bunge\*

*A<sup>3</sup> by Airbus, Santa Clara, CA, U.S.A.*

Marco Pavone<sup>†</sup>, Ilan M. Kroo<sup>‡</sup>

*Stanford University, Stanford, CA, U.S.A.*

In a pullout maneuver an initially diving aircraft is returned to level flight. Depending on the initial condition, aircraft characteristics and control inputs, altitude loss may be significant and minimizing it can be important to avoid collision with the ground. A motivating example is that of stall/spin recoveries, where the pullout represents a majority of the total altitude lost. This paper presents a solution of the minimal altitude loss pullout maneuver by posing it as an infinite horizon optimal control problem and solving it using dynamic programming techniques on a reduced-order point mass model for a low-wing general aviation aircraft. The computed optimal policy results in a “bang-bang” type controller, typical of shortest path problems, with maximum lift coefficient and bank rate applied at each point in time. The effect of maximum lift coefficient on the minimum altitude loss is analyzed, showing that attaining the highest lift coefficient possible throughout the pullout is critical. Based on these results a pullout flight control system is designed, with the optimal policy acting as an outer loop issuing commands to two inner loops that track lift coefficient and roll rate, respectively. The proposed pullout controller is tested on 6 DOF simulations, and shown to be effective at recovering the aircraft with close to optimal altitude loss.

## Nomenclature

|  |   |
|--|---|
| $\rho$   | air density   |
| $b$  | wing span   |
| $c$  | chord length  |
| $S$  | wing surface area   |
| $p_x, p_y, p_z$                                  | northward, eastward and down position                               |
| $h$  | altitude, from the ground   |
| $u, v, w$  | body-x, y and z velocity  |
| $V$  | airspeed  |
| $\alpha$   | angle of attack   |
| $\beta$  | sideslip angle  |
| $\phi, \theta, \psi$                             | roll, pitch and yaw angles  |
| $\gamma$   | flight path angle   |
| $\mu$  | bank angle  |
| $\epsilon_0, \epsilon_1, \epsilon_2, \epsilon_3$ | Euler parameters  |
| $p, q, r$  | roll, pitch and yaw rate  |
| $\delta e$                                       | elevator deflection, positive trailing edge down                    |
| $\delta r$                                       | rudder deflection, positive trailing edge to the left               |
| $\delta a$                                       | aileron deflection, positive is trailing edge down of right aileron |
| $\delta t$                                       | throttle position   |
| $\hat{p}$  | dimensionless roll rate, $\hat{p} = \frac{pb}{2V}$                  |
| $L, D, Y$  | aerodynamic lift, drag and side force                               |

---

\*Flight Simulation and Control Engineer, Project Vahana, AIAA Member.

<sup>†</sup>Assistant Professor, Department of Aeronautics and Astronautics, AIAA Member

<sup>‡</sup>Professor, Department of Aeronautics and Astronautics, AIAA Fellow.

|                 |  |
|-----------------|--|
| $M_x, M_y, M_z$ | aerodynamic rolling, pitching and yawing moment about the c.g.             |
| $C_L, C_D, C_Y$ | aerodynamic lift, drag and side force coefficient                          |
| $C_l, C_m, C_n$ | aerodynamic rolling, pitching and yawing moment coefficient about the c.g. |
| f               | system dynamic equation of motion  |
| J               | value function   |
| g               | stage cost   |
| a               | vector of actions  |

## I. Introduction

### A. Motivation

In a pullout maneuver, also called a dive recovery or pull-up, the goal is to return the aircraft to level flight from an initially diving condition. Depending on the initial condition, aircraft characteristics and control inputs applied the altitude loss may be substantial, in the order of tens to hundreds of wing spans, and minimizing altitude loss is an important metric for several flight scenarios. In particular, for stall/spin recoveries, minimizing the altitude loss in the pullout phase is critical to avoid collision with the ground. For example, for the Grumman American AA-1 Yankee tested by NASA,<sup>1</sup> the pullout altitude represents approximately 65 % of the total altitude loss for one turn spins, and more than 90 % for spin recoveries initiated at or before half a turn.<sup>2</sup> Thus, having a flight control system that minimizes pullout altitude is a central piece in an automatic spin recovery system. This paper investigates minimum altitude pullout maneuvers, using the Grumman American AA-1 Yankee as an example case, and proposes a feedback controller that accomplishes this.

### B. Previous Research

Minimal altitude loss maneuvers have been studied in the past in different contexts and using varied techniques. Probably the earliest work is that by Lanchester,<sup>3</sup> who developed the “phugoid equation” and “phugoid curves” where a constant lift coefficient and no drag were assumed, showing that the altitude required to reach level flight by an aircraft initially at rest and pointing vertically downwards is three times the altitude it takes to reach the stall speed in free vertical fall. The work by R.T. Jones<sup>4</sup> concerning pitch effectiveness requirements for minimum altitude dive recoveries in hang gliders further extended these ideas by including drag, as well as pitch dynamics, and numerically calculating the flight paths. Vinh<sup>5</sup> posed the minimum altitude pullout maneuver as an optimal control problem, and numerically solved it for the case of bounded lift coefficient with calculus of variations techniques. Shultz et al.<sup>6</sup> proposed a methodology to solve different kinds of minimal time three dimensional maneuvers, based on Euler-Lagrange optimization theory and energy state approximations. In this work the control variables were thrust, angle of attack and roll angle, thus neglecting roll dynamics. More recently, Garcia et al.<sup>7</sup> developed an algorithm that computes the controls required to return the aircraft to level flight from “unusual attitudes” caused by a loss of control event, by posing it as a free final time optimal control problem, which is solved numerically by minimizing a cost function. The problem is re-solved in a receding horizon fashion, with only the first control input applied at each time step. The cost being optimized is not altitude loss, but error of the final state with respect to level flight.

The contributions of this paper are threefold. Firstly, the aircraft dynamics are not restricted to symmetric flight, nor small angles, and incorporate the fact that the bounds on lift coefficient (stall) are not symmetric for positive and negative angles of attack. Indeed, this leads to surprising results, whereby for certain initial conditions the optimal maneuver involves rolling over and effecting inverted pullout recoveries. Secondly, this study solves for a stationary feedback control system, rather than an open loop policy, making it more robust to initial conditions and disturbances, while avoiding the need for costly online optimizations, making it relatively easy to implement on modern flight systems. Lastly, the designed control system is tested on full nonlinear 6 DOF simulations, demonstrating its effectiveness.

## II. Problem Formulation

The minimal altitude pullout can be expressed mathematically as a fixed final state, variable final time, optimal control problem, as in Equation 1, which could be solved using direct methods, such as collocation trajectory optimization, or calculus of variations techniques. The shortcoming of these approaches is that they only provide a set of open loop control inputs for a specific initial condition. By noting that the objective function is the integral of a function of the states, the minimization can be cast as an infinite horizon dynamic programming problem with an absorbing state at level flight, as shown in Equation 2. With this approach the solution not only provides the minimum altitude loss, but also the optimal policy, as a function of the current state, enabling feedback control.

$$\begin{aligned}
 h^*(x_0) &= \min_{a(t), t_f} \int_0^{t_f} -V \sin \gamma dt \\
 \text{s.t.} \quad & \dot{x} = f(x, a) \\
 & x(0) = x_0 \\
 & \gamma(t_f) = 0
 \end{aligned} \tag{1}$$

$$\begin{aligned}
 h^*(x_0) &= \min_{a(t)} \int_0^{\infty} -V \sin \gamma dt \\
 \text{s.t.} \quad & \dot{x} = \begin{cases} f(x, a), & \text{if } \gamma < 0 \\ 0 & \text{if } \gamma \geq 0 \end{cases}
 \end{aligned} \tag{2}$$

## III. Optimal Policy with Reduced Order Dynamics

The dynamic programming problem in Equation 2 can be solved numerically with techniques such as value iteration,<sup>8</sup> by discretizing the state and control space. A significant challenge is that the full equations of motion shown in Appendix A, have eight states and 3 control inputs ( $\delta e$ ,  $\delta a$  and  $\delta r^a$ ), and if for example each state were discretized into 10 bins, and the control inputs into 5 bins, there would be a total of  $1.25 \times 10^{10}$  grid points making the required computational resources prohibitive. Thus, a lower order approximate dynamic representation is sought.

Assuming lift coefficient  $C_L$  and bank rate  $\dot{\mu}$  are controlled by inner loops using the elevator and aileron respectively, whereby the closed loop  $C_L$  and bank rate response is of high enough bandwidth that their dynamics can be neglected, that the sideslip angle remains close to zero, that the drag coefficient  $C_D$  is only a function of lift coefficient, and the side force coefficient  $C_Y$  is small enough to be neglected, then the equations of motion in Appendix A.2 simplify to Equation 3.

$$\dot{V} = -g \sin \gamma - 1/2 \rho \frac{S}{m} V^2 C_D(C_L^{cmd}) \tag{3a}$$

$$\dot{\gamma} = 1/2 \rho \frac{S}{m} V C_L^{cmd} \cos \mu - \frac{g}{V} \cos \gamma \tag{3b}$$

$$\dot{\mu} = \dot{\mu}^{cmd} \tag{3c}$$

To avoid stall, the control input  $C_L^{cmd}$  should be limited to stay within a safety margin with respect to the maximum lift coefficient. For the Grumman American AA-1 Yankee, the aircraft studied in this paper, the positive stall  $C_L$  is 1.2,<sup>9</sup> while the negative stall  $C_L$  (at negative angle of attack) can be approximated as -0.7 (calculated from the section lift curve shown in 10). Setting a margin of 0.2 with respect to stall (which is a margin of 2.5 deg with respect to the stall angle of attack), the positive and negative  $C_L^{cmd}$  limits are 1.0 and -0.5 respectively, as shown in Equation 4. It should be noted that during a pullout maneuver, in which there is a positive pitch rate the effects of induced camber may actually increase the maximum  $C_L$  above the static value just mentioned. Since this effect is neglected in this investigation, the results here obtained

<sup>a</sup>This investigation is limited to idle power maneuvers, so  $\delta t$  is not a control input.

are actually conservative. The same can be said of the effect of flaps and power, which as shown in Ref. 9 can increase maximum  $C_L$  to as much as 1.45.

The bank rate command  $\dot{\mu}_{cmd}$  is constrained by the aircraft dynamics, the limits of which can be approximated by the steady state roll rate with maximum aileron deflection. From estimates of the roll damping and aileron effectiveness, and a reference airspeed it is possible to calculate such a roll rate. Choosing the reference speed to be the stall speed results in a conservative value for the maximum roll rate, as in Equation 5. For the Grumman Yankee  $C_{l_p} \approx -0.5$  and  $C_{l_{\delta a}} \approx -0.0595$  1/deg (from Ref. 11),  $\delta a_{max} = 25$  deg,  $b = 7.41$  m and the stall speed is approximately 32 m/s, resulting in a maximum roll rate of  $p_{max} \approx 30$  deg/s.

$$-0.5 \leq C_L^{cmd} \leq 1.0 \quad (4)$$

$$|\dot{\mu}_{cmd}| \leq \dot{\mu}_{max} \approx p_{max} \quad (5a)$$

$$p_{max} \approx \hat{p}_{max} \frac{2V_{ref}}{b} = \left| \frac{C_{l_{\delta a}}}{C_{l_p}} \right| \delta a_{max} \frac{2V_{ref}}{b} \quad (5b)$$

The state-control space is discretized into a rectangular grid with uniform spacing in each of the dimensions, as shown in Table 1, and time is discretized with a time step of 0.1 seconds. The optimal value function must satisfy the Bellman Equation (Equation 6), and can be found by applying the recursive value iteration algorithm, since it is a fixed point of this equation, where  $g(x, a) = -V \sin \gamma \Delta t + 0.01 \dot{\mu}_{cmd}^2$ . The extra term was added to the stage cost function to smooth out the bank rate command optimal policy, which would otherwise be jagged.

**Table 1. Discretization of state-control space ( $V_s$ : stall speed).**

| Variable          | Lower Bound | Increment | Upper Bound | Units    |
|-------------------|-------------|-----------|-------------|----------|
| V                 | 0.9         | 0.1       | 4.0         | 1/ $V_s$ |
| $\gamma$          | -180        | 5         | 0           | deg      |
| $\mu$             | -20         | 5         | 200         | deg      |
| $C_L^{cmd}$       | -0.5        | 0.25      | 1.0         | -        |
| $\dot{\mu}^{cmd}$ | -30         | 5         | 30          | deg/s    |

$$J^*(x) = \min_{a \in A} \{g(x, a) + J^*(x'(x, a))\} \quad (6)$$

---

**Algorithm 1** Value Iteration

---

- 1:  $k = 1$
  - 2:  $J_1(x) = \min_a g(x, a)$
  - 3: **while** converged = 0 **do**
  - 4:      $J_{k+1}(x) = \min_u \{g(x, a) + J_k(x'(x, a))\}$
  - 5:     converged =  $\text{convcrit}(J_k, J_{k+1})$
  - 6:      $k = k+1$
  - 7:  $J^*(x) = J_k(x)$
  - 8:  $a^*(x) = \text{argmin}_a \{g(x, a) + J^*(x'(x, a))\}$
  - 9: **return**  $J^*, a^*$
- 

Applying Algorithm 1 we obtain the optimal value function and policy, shown in Figures 1 and 2, respectively. The optimal policy for both  $C_L^{cmd}$  and  $\dot{\mu}_{cmd}$  exhibit a “bang-bang” type control, whereby the control inputs go from one extreme to the other upon crossing a switching surface. This is common for

shortest path optimal control problems,<sup>12</sup> in which applying maximum allowable control authority at all times drives the system to the terminal state fastest and with minimal cost. In this case, because the limits on  $C_L$  are not symmetric, the optimal policy is not symmetric about the 90 deg bank angle.

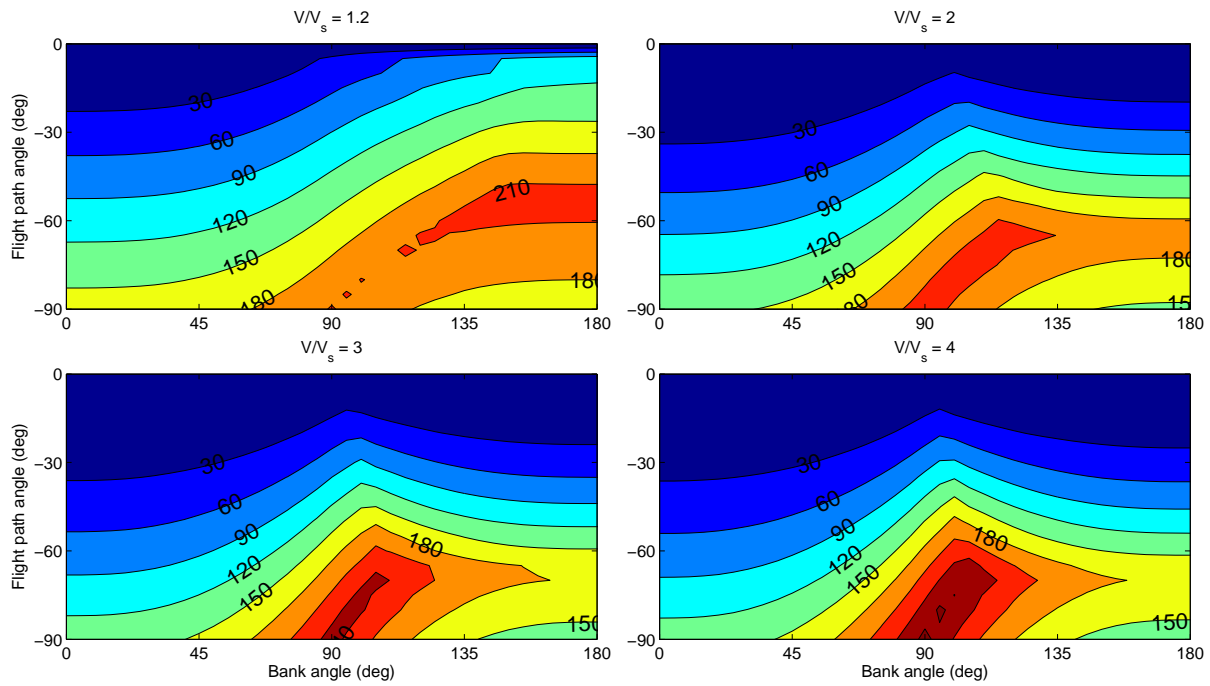


Figure 1. Minimum pullout altitude loss as a function of bank and flight path angle, for different normalized airspeeds. Going clockwise starting for the top left, these correspond to  $\frac{V}{V_s} = 1.2, 2, 4$  and  $3$ , respectively.

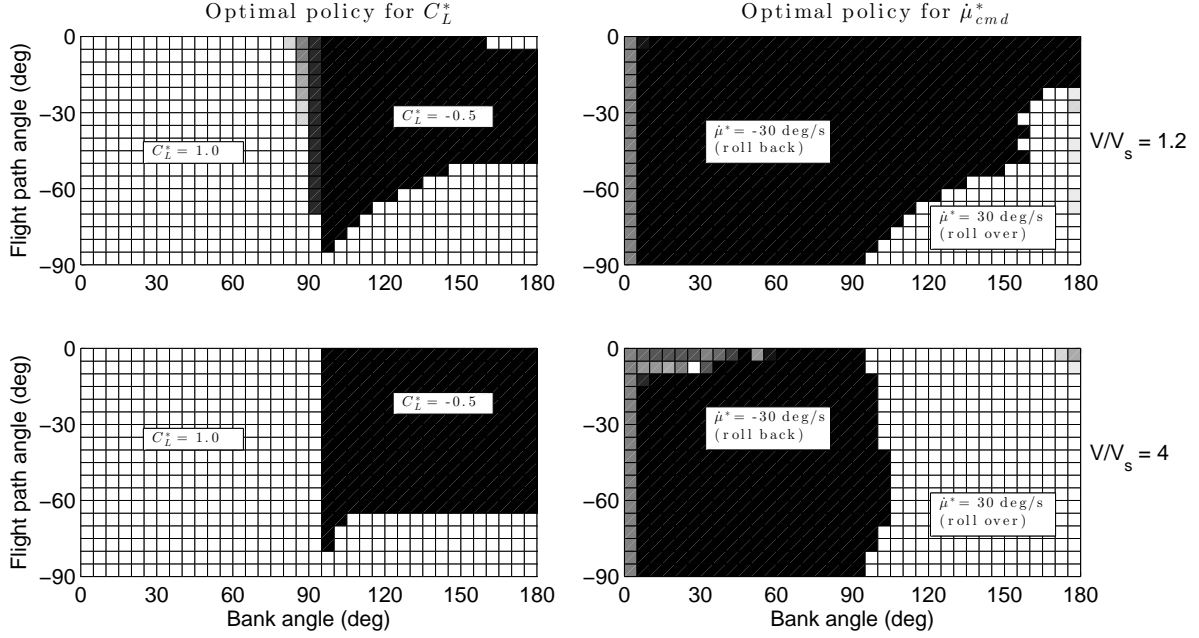


Figure 2. Optimal  $C_L^{cmd}$  and  $\dot{\mu}^{cmd}$  as a function of bank and flight path angle, for different normalized airspeeds. The top figures correspond to  $\frac{V}{V_s} = 1.2$ , while the bottom ones to  $\frac{V}{V_s} = 4$ . The white and black coloring indicate if the optimal input is positive or negative (also noted in the white text boxes), with the edges of the white-black regions defining the switching surfaces.

To better visualize the resulting policy, optimal trajectories are simulated starting from different initial conditions. Figure 3 shows optimal pullouts from a stall relative initial airspeed of 1.2, initial flight path angle of -30 deg, and initial bank angles of 30, 60, 90, 120 and 150 deg. As the initial bank increases altitude loss grows almost four fold, from  $\approx 40$  m at  $\mu = 30$  deg, to over 150 m at  $\mu = 150$  deg. Moreover, at  $\mu = 150$  deg (i.e. when the aircraft is almost inverted) the optimal action is to apply negative  $C_L$  (i.e. stick forward) and perform an inverted pullout instead of rolling back to an upright attitude and then pulling up.

Figure 4 shows a similar set of trajectories, but starting from a steeper flight path angle ( $\gamma_0 = -60$  deg). Again, as the initial bank angle increases so does altitude loss, with a two fold increase. A break in the optimal trajectory is also observed when close to inverted flight, although in this case, instead of remaining inverted, the aircraft rolls over reaching a vertical attitude and then pulls up to an upright attitude.

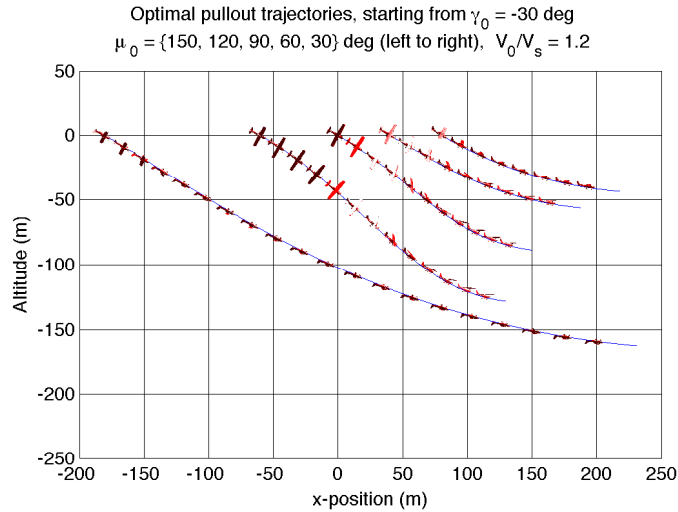


Figure 3. Optimal pullout trajectories for  $\gamma(0) = -30$  deg.

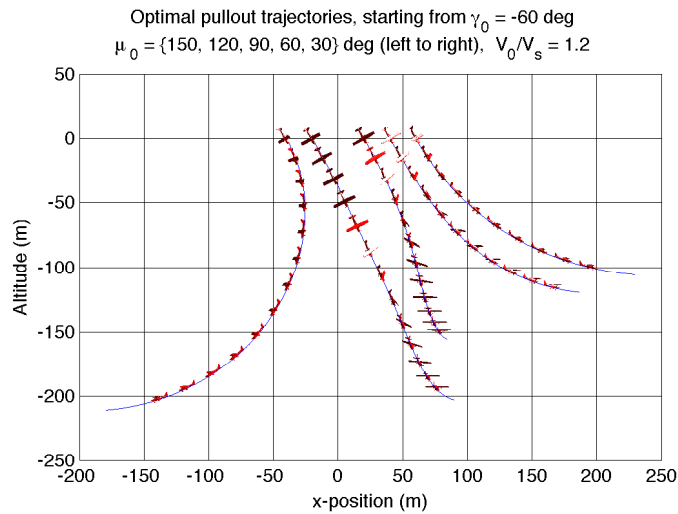


Figure 4. Optimal pullout trajectories for  $\gamma(0) = -60$  deg.

#### IV. Pullout Altitude Loss and Maximum Lift Coefficient

The minimum pullout altitude loss is directly related to the maximum lift coefficient achievable by the controller. The higher this is, the more capacity the aircraft has to turn the trajectory upwards and hence to reduce altitude loss. Figure 5 shows the relation between  $C_{Lmax}^{controller}$ , the maximum lift achieved by an inner loop controller, and the increment in pullout altitude loss as compared with a controller that can reach  $C_L = 1$ . The shown curves correspond to pullouts starting from  $V_0 = V_{stall}$ ,  $\mu_0 = 60$  deg and for three different initial flight path angles,  $\gamma_0 = -90, -60, -30$  deg. As is evident, there is a notable cost if the achievable  $C_L$  is below 1. For example, when starting from a dive angle of 60 deg, if the  $C_L$  during the pullout is 0.8 there is an increment of almost 30 meters. This motivates the design of a controller that can reach  $C_L = 1$  while ensuring that the stall  $C_L$  is not surpassed, the topic of the next section. Figure 5 also highlights how mechanisms that increase stall  $C_L$  could enable further reductions in altitude loss. For

example, if flaps are deployed and power applied  $C_{L_{stall}}$  can be increased to 1.45. With a safety margin of 0.2 on  $C_L$ , for an initial dive angle of 60 deg this would mean a reduction of about 20 meters.

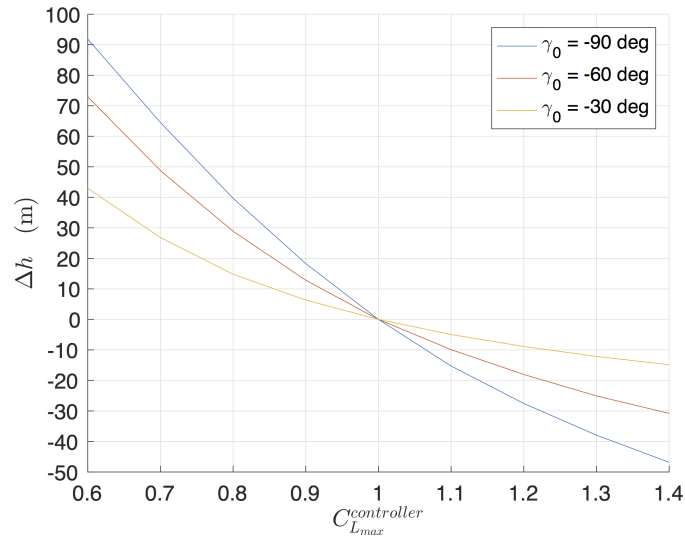


Figure 5. Variation of minimum pullout altitude loss with  $C_{L_{max}}$

## V. Pullout Controller

### A. Controller Architecture

The pullout controller consists of an outer loop issuing lift coefficient and bank rate commands, based on the optimal policy computed in the previous section, which are tracked by two inner controllers. The following sections address the design of such inner controllers by analyzing the open-loop linearized dynamics, and designing feedback controllers that achieve fast response while remaining within the bounds protecting against secondary stalls. To simplify the controller, rudder is left neutral since the open loop directional stability maintains the sideslip angle sufficiently close to zero without significant impact on the maneuvers. The proposed controller assumes the availability of flight path angle and lift coefficient estimates. The latter could be estimated from accelerometer and airspeed measurements. The design of such estimators and the analysis of effects of noise is beyond the scope of the present investigation.

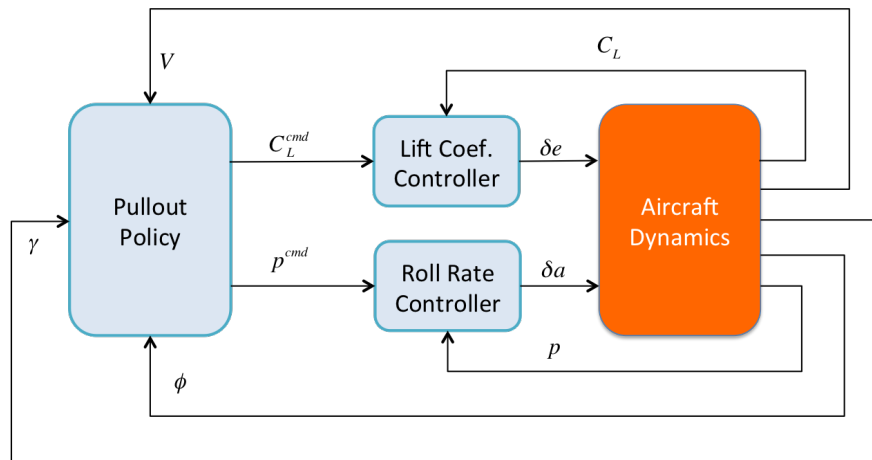


Figure 6. Pullout controller architecture.

## B. Lift Coefficient Controller

### 1. Nonlinear Longitudinal Dynamics

To simplify the analysis of the lift controller, symmetric conditions are assumed. Using the “Flow and Euler Angle” representation of the equations of motion in appendix A.3 , the nonlinear equations of motion are shown in Equation 7. The linearized aerodynamic model described in Appendix B is used for this analysis.

$$\dot{V} = -g \sin(\theta - \alpha) - \frac{1/2\rho S}{m} V^2 C_D \quad (7a)$$

$$\dot{\alpha} = q - \frac{1/2\rho S}{m} V C_L + \frac{g}{V} \cos(\theta - \alpha) \quad (7b)$$

$$\dot{\theta} = q \quad (7c)$$

$$\dot{q} = \frac{1/2\rho S c}{I_{yy}} V^2 C_m \quad (7d)$$

### 2. Quasi-steady Pullout Relations

In a pullout, quasi-steady relations can be established between the different variables. For a given elevator deflection, airspeed and flight path angle, the corresponding quasi-steady angle of attack and pitch rate can be computed by enforcing  $\dot{\alpha} = \dot{q} = 0$ . These are only quasi-steady because as the pullout progresses the airspeed and flight path angle change, albeit at a slow rate compared to angle of attack and pitch rate. As Figure 7(a) shows, the quasi-steady angle of attack and lift coefficient are almost exclusively a linear function of elevator deflection. When computing these relations the stall limits ( $C_L \in (-0.7, 1.2)$ ) were imposed as constraints, so the white spaces indicate stall regions. For shallow dive angles, the pitch rate is mostly exclusively a function of the elevator deflection, as shown in Figure 7(c), while for steep dives, flight path angle also starts to affect it, with the quasi-steady pitch rate increasing as the dive steepens. These quasi-steady relations can be inverted, such that for a given state and target  $C_L$  the corresponding steady state elevator deflection and pitch rate can be computed. These can be leveraged in the feedforward paths of the  $C_L$  controller enabling zero steady-state command tracking error, rather than relying on an integrator which can cause dangerous overshoots.

The relation between steady/quasi-steady  $C_L$  and  $\delta e$ , shown in Figure 7(d), is actually very similar during steady pullouts and glides, indicating that this relation could be determined experimentally by performing steady glides at different airspeeds. Since the  $C_L$  during the pullout is smaller than that of the glides, this is a conservative approach, ensuring that stall is not inadvertently reached. With further knowledge of aerodynamic parameters, such as  $C_{m_q}$ , the glide relations can be appropriately modified to get closer to the pullout relations. An alternative approach could include actually performing pullouts and establishing this relation directly.

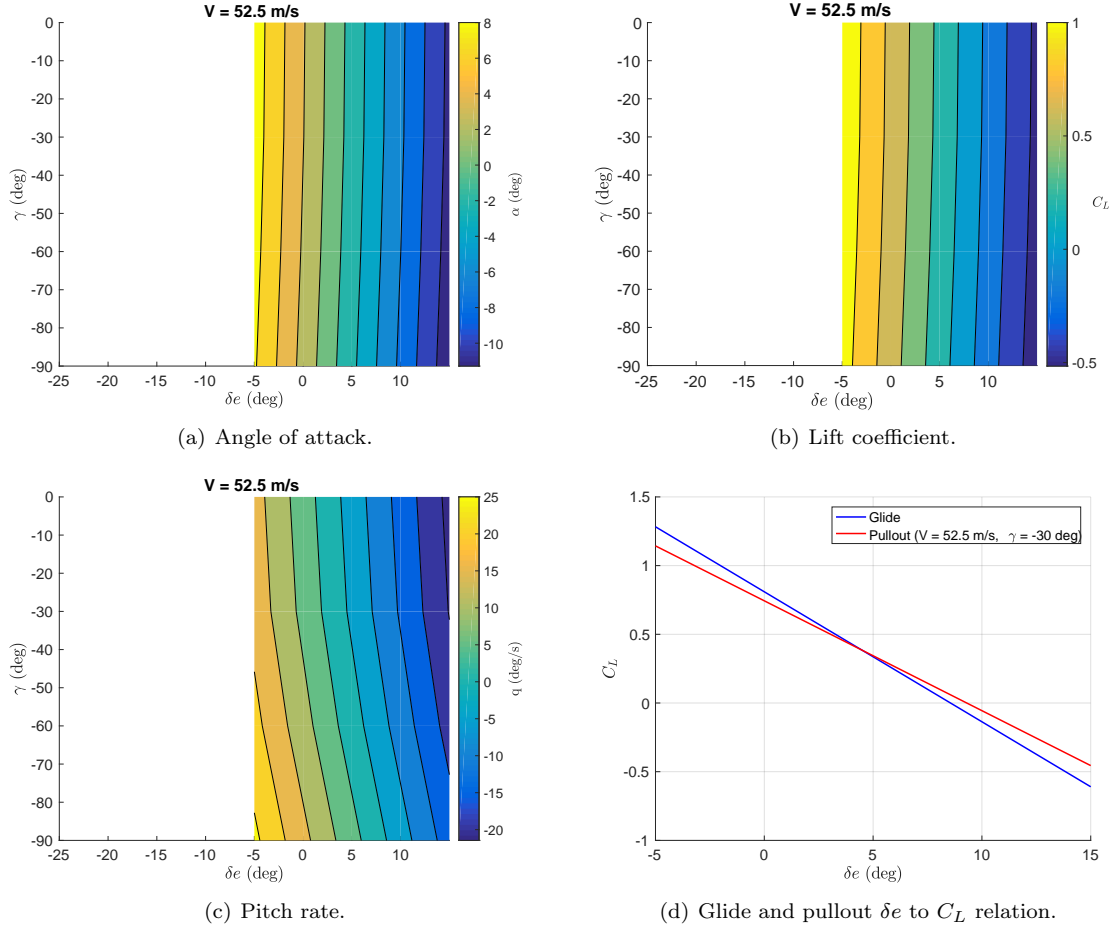


Figure 7. Quasi-steady longitudinal relations.

### 3. Linearized Longitudinal Dynamics

Linearizing about a quasi-steady pullout condition  $V_0, \alpha_0, \theta_0, q_0, \delta e_0$  a state space representation  $\dot{X}' = AX' + B\delta e'$  is obtained<sup>b</sup>, with the  $A$  and  $B$  matrices given in Equation 8, where  $\gamma_0 = \theta_0 - \alpha_0$ ,  $k_1 = 1/2\rho\frac{S}{m}$  and  $k_2 = \frac{\rho S c V_0^2}{2I_{yy}}$ .

$$A = \begin{bmatrix} -2k_1 V_0 \bar{C}_D & g \cos \gamma_0 - k_1 V_0^2 (C_{D1} + 2C_{D2} \alpha_0) & -g \cos \gamma_0 & 0 \\ -k_1 \bar{C}_L - \frac{g}{V_0^2} \cos \gamma_0 & -k_1 V_0 C_{L\alpha} + \frac{g}{V_0} \sin \gamma_0 & -\frac{g}{V_0} \sin \gamma_0 & 1 \\ 0 & 0 & 0 & 1 \\ 2k_2 (V_0 \bar{C}_m - \frac{c}{4} C_{m_q} q_0) & \frac{k_2}{2} V_0^2 C_{m_\alpha} & 0 & \frac{k_2}{2} V_0 C_{m_q} \end{bmatrix} \quad (8a)$$

$$B = \begin{bmatrix} 0 \\ 0 \\ 0 \\ k_2 V_0^2 C_{m_{\delta e}} \end{bmatrix} \quad (8b)$$

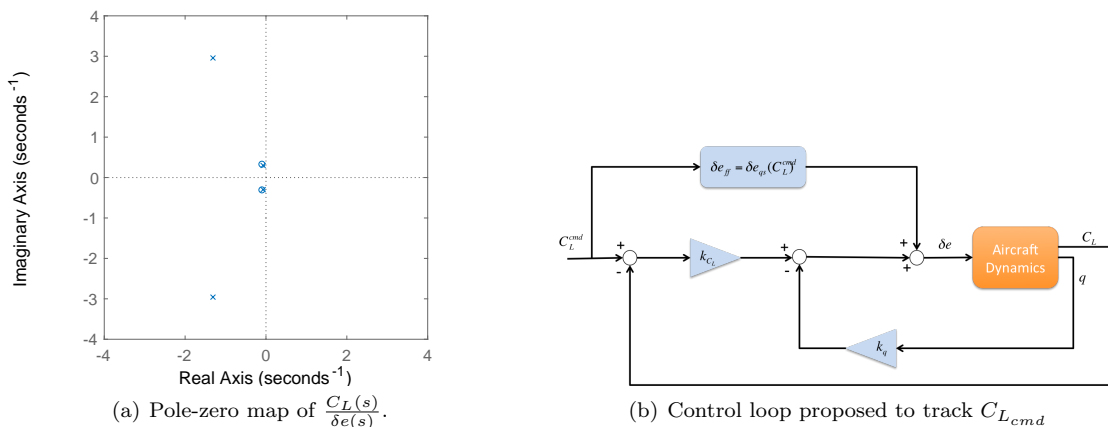
### 4. Controller Design

As was shown in Section IV, maximizing  $C_L$  is a vital part of minimizing altitude loss. The challenge is to do this while ensuring that a secondary stall does not occur (i.e.  $-0.7 \leq C_L < 1.2$ ). The dynamics from

<sup>b</sup> $X'$  and  $\delta e'$  are perturbational quantities about the quasi-steady values

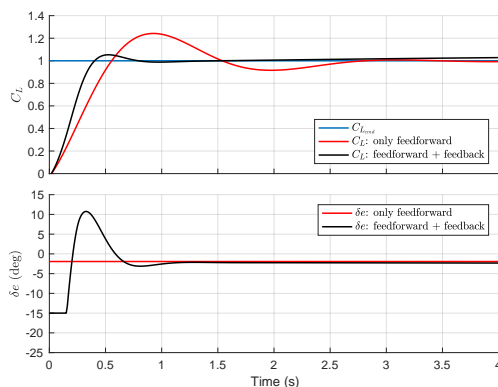
elevator to  $C_L$  are dominated by the short period mode (much like the angle of attack) which on tailplanes is usually fast and well damped compared to the phugoid mode. Figure 8(a) shows the zero-pole map of the open loop transfer function  $\frac{C_L(s)}{\delta e(s)}$ . The zeros near the phugoid poles tend to cancel this mode out, leaving the short period poles as dominant, as previously mentioned. The natural frequency and damping ratio of these are 3.24 rad/s and 0.41 respectively, corresponding to a rise time of 0.53 seconds and overshoot of 25%. For scenarios in which every meter counts, such as stall/spin recovery, there might be room for improvement over the open loop dynamics, and thus a feedback controller is proposed, as shown in Figure 8(b).

The feedforward path is essentially the inversion of the quasi-steady relations previously presented, which can be found either from modeling or experimentally or a combination of both. In the present analysis we use the model available to compute this. Gain  $k_{C_L}$  is chosen to increase the bandwidth of the closed loops system, while  $k_q$  to increase the damping, and thus control overshoot. It should be noted that the pitch rate shown in the feedback path is actually the difference between the measured and the quasi-steady pitch rate as calculated using the above relations. Since the target  $C_{L_{cmd}}$  issued by the outer loops is 1.0, and the stall  $C_L$  is 1.2, we set the maximum allowable overshoot of 0.05 (5 %), leaving a margin of 0.15 with respect to stall. A discussion of robustness to modeling uncertainty and external disturbances is probably warranted given the high cost of secondary stalls, but is excluded from the scope of this investigation.



(a) Pole-zero map of  $\frac{C_L(s)}{\delta e(s)}$ .

(b) Control loop proposed to track  $C_{L_{cmd}}$



(c)  $C_L$  step response.

**Figure 8. Open loop pole-zero map, feedback loop and response for the lift coefficient controller.**

Figure 8(c) shows an overlay of the uncompensated (just feedforward) and compensated (feedforward and feedback)  $C_L$  response. As can be seen, the uncompensated response is not ideal since for a steady state  $C_L = 1$  the overshoot goes above the stall limit. In practice, this means that the maximum  $C_L$  that can be safely targeted is below 1 (probably nearer to 0.8). The compensated response on the other hand is well damped keeping the overshoot within the 0.05 limit. It is also faster, with a rise time of  $\sim 0.4$  seconds. In the response shown the elevator is limited to -15 to 15 deg. An important challenge for the feedback loop

proposed is having a good estimate of  $C_L$ . Provided there are accelerometer and airspeed measurements, the lift coefficient can be approximated as  $C_L \approx \frac{ma_z}{1/2\rho SV^2}$ . In practice, some filtering would be necessary to reduce the effect of sensor noise, and thus some lag would be added. If no airspeed data was available, a similar loop based on feeding back normal acceleration could be implemented instead (i.e. tracking g's instead of  $C_L$ ).

### C. Roll Rate Controller

For small  $\alpha$  and  $\beta$ , the bank angle is approximately equal to the roll angle, and thus the bank rate command  $\dot{\mu}_{cmd}$  issued by the optimal pullout policy can be achieved by tracking roll rate instead.

#### 1. Nonlinear Lateral Dynamics

To simplify the analysis it is assumed that the longitudinal flight variables are quasi static. The resulting nonlinear lateral equations of motion are shown in Equation 9. As in the previous section, the aerodynamic model in Appendix B is used.

$$\dot{\phi} = p + (q \sin \phi + r \cos \phi) \tan \phi \quad (9a)$$

$$\dot{p} = \frac{1/2\rho V^2 S b C_l}{I_{xx}} - qr \frac{(I_{zz} - I_{yy})}{I_{xx}} \quad (9b)$$

$$\dot{r} = \frac{1/2\rho V^2 S b C_n}{I_{zz}} - qp \frac{(I_{yy} - I_{xx})}{I_{zz}} \quad (9c)$$

$$\begin{aligned} \dot{\beta} &= \frac{1/2\rho V^2 S (C_D \sin \beta + C_Y \cos \beta)}{mV} - (r \cos \alpha - p \sin \alpha) \\ &+ \frac{g}{V} [\cos \theta \sin \phi \cos \beta + (\cos \alpha \sin \theta - \sin \alpha \cos \theta \cos \phi)] \end{aligned} \quad (9d)$$

#### 2. Linearized Lateral Dynamics

The system is linearized about  $\beta = p = r = 0$  and  $\phi = \phi_0$ , resulting in a state-space representation  $\dot{X}' = AX' + B\delta'_a$  with  $A$  and  $B$  matrices as shown in Equation 10, where  $k_3 = 1/2\rho V^2 S$  and  $k_4 = \frac{g}{V}(\cos \alpha \sin \theta - \sin \alpha \cos \theta \cos \phi_0)$ .

$$A = \begin{bmatrix} q \cos \phi_0 \tan \theta & 1 & \cos \phi_0 \tan \theta & 0 \\ 0 & \frac{k_3 b^2}{2V I_{xx}} C_{l_p} & \frac{k_3 b^2}{2V I_{xx}} C_{l_r} - q \frac{(I_{zz} - I_{yy})}{I_{xx}} & \frac{k_3}{I_{xx}} C_{l_\beta} \\ 0 & \frac{k_3 b^2}{2V I_{zz}} C_{n_p} - q \frac{(I_{yy} - I_{xx})}{I_{zz}} & \frac{k_3 b^2}{2V I_{zz}} C_{n_r} & \frac{k_3}{I_{zz}} C_{n_\beta} \\ \frac{g}{V} \cos \theta \cos \phi_0 & \frac{k_3 b}{2mV^2} C_{Y_p} + \sin \alpha & \frac{k_3 b}{2mV^2} C_{Y_r} - \cos \alpha & \frac{k_3}{mV} C_{Y_\beta} + \frac{D}{mV} + k_4 \end{bmatrix} \quad (10a)$$

$$B = k_3 \begin{bmatrix} 0 & 0 \\ \frac{b C_{l_{\delta a}}}{I_{xx}} & \frac{b C_{l_{\delta r}}}{I_{xx}} \\ \frac{C_{Y_{\delta a}}}{mV} & \frac{C_{Y_{\delta r}}}{mV} \end{bmatrix} \quad (10b)$$

Figure 9(a) shows the pole zero map of the transfer function from aileron to roll rate, for the flight condition  $V = 35$  m/s,  $\theta = -55$  deg,  $\alpha = 8$  deg/s,  $\phi_0 = 50$  deg. As was the case for  $C_L$ , the roll rate transfer function has two lightly damped modes that have zeros nearby, effectively removing these from the response, and a very slow stable real mode also canceled by a zero, leaving only the highly damped and fast roll subsidence mode. This makes it very easy to control roll rate with a simple proportional gain from roll rate error to aileron, and an input shaping gain to reduce steady-state command tracking error. Choosing the gains such that the ailerons reach their limits when the roll rate error is 30 deg/s gives the step response shown in Figure 9(b), where the command was 30 deg/s. The response is very fast with a rise time in the order of 0.1 seconds, and has minimal overshoot. Given the good performance achieved with this simple controller, no further improvement is sought.

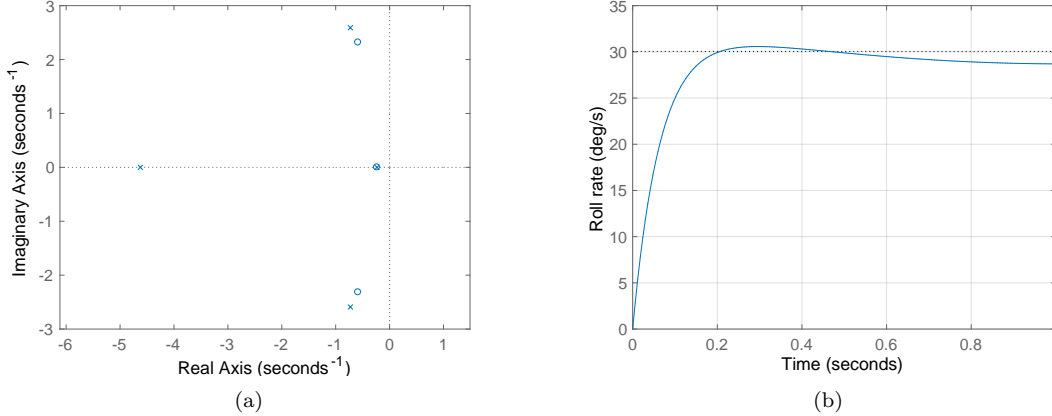


Figure 9. Pole-zero map of open loop transfer function from aileron to roll rate, and closed loop roll rate step response.

## VI. 6 DOF Pullout Simulations

This section analyzes the effectiveness of the proposed controller to execute pullout maneuvers by simulating recoveries with the full 6 DOF equations of motion. The simulations are done with the “Body Velocity and Quaternions” representation described in appendix A.1 and the aerodynamic model in appendix B. In addition, the recoveries are compared with optimal pullout maneuvers on the 3 DOF dynamic model presented in Section III. Figure 10 shows an example pullout maneuver starting from a dive angle of 60 degrees, roll angle of 30 degrees, airspeed 1.1 times that of stall and zero angle of attack, side slip angle and angular rates. As can be seen, the controller indeed returns the aircraft to level flight. Moreover, the details of the trajectory, and in particular the altitude loss, closely match that of the 3 DOF optimal policy. Figure 10 compares the altitude loss from the 6 DOF and 3 DOF simulations for a range of initial dive and bank angles (with the rest of the states in the aforementioned values). For bank angles less than 65 degrees the difference in altitude loss is less than 5 meters, and the relative difference less than 5% (there is a small region at  $\gamma_0 = -30$  deg and  $\mu_0 \leq 5$  deg where the relative difference is  $\sim 10\%$ ). The same can be said of dive angles less than 50 degrees. As the 90 degrees banked vertical dive ( $\gamma_0 = -90$  deg,  $\mu_0 = 90$  deg) is approached, the altitude difference grows progressively, reaching a maximum of 41 meters and 25% at that point. As can be seen in Figure 12, showing the trajectories from a 90 degrees banked vertical dive, the trajectories differ significantly. Particularly noteworthy is the bank angle trajectory<sup>c</sup>. In the 6 DOF model the quaternion attitude representation correctly handles the fact that this is actually a straight pullout, with the bank angle immediately returning to zero, while the 3 DOF simulation does not handle the singularity correctly, returning to wings level attitude at the prescribed maximum bank angle rate of 30 deg/s. Given the slow reduction in bank angle in the 3 DOF dynamic model, the flight path angle also changes at a slower pace (note the  $\cos \mu$  in Equation 3b for  $\dot{\gamma}$ ), resulting in the larger altitude loss. This highlights a shortcoming of the 3 DOF reduced order model at the perfectly vertical dive angle (i.e.  $\gamma = \pm 90$  deg). In fact, if we look at the “Flight Path and Flow angle” equations of motion shown in Appendix A.2, the bank rate equation has a singularity at  $\gamma = \pm 90$  degrees due to the presence of  $\tan \gamma$ . Future investigations could include the term  $\sin \mu \tan \gamma \frac{L}{mV}$  in the bank rate equation of the 3 DOF dynamic model, and see if this reduces the mismatch in altitude loss with the 6 DOF model. Special treatment of the equations will be necessary if  $\gamma = -90$  degrees is to be included in the state-space domain of the dynamic programming problem, to eliminate or alleviate the singularity.

Notwithstanding the observations on the shortcoming of the 3 DOF model, it is important to return to the original question, and point out that the pullout controller reliably recovers the aircraft from the dive, with an altitude loss very close to the minimum predicted by the optimal policy.

<sup>c</sup>It should be noted that due to the trigonometric symmetry of the flight path-bank angle representation, flight path angles below -90 degrees, are equal to their 180 deg complement in both flight path angle and bank angle, making the trajectories shown in Figure 12 physically very similar, although the curves evolve in opposite directions.

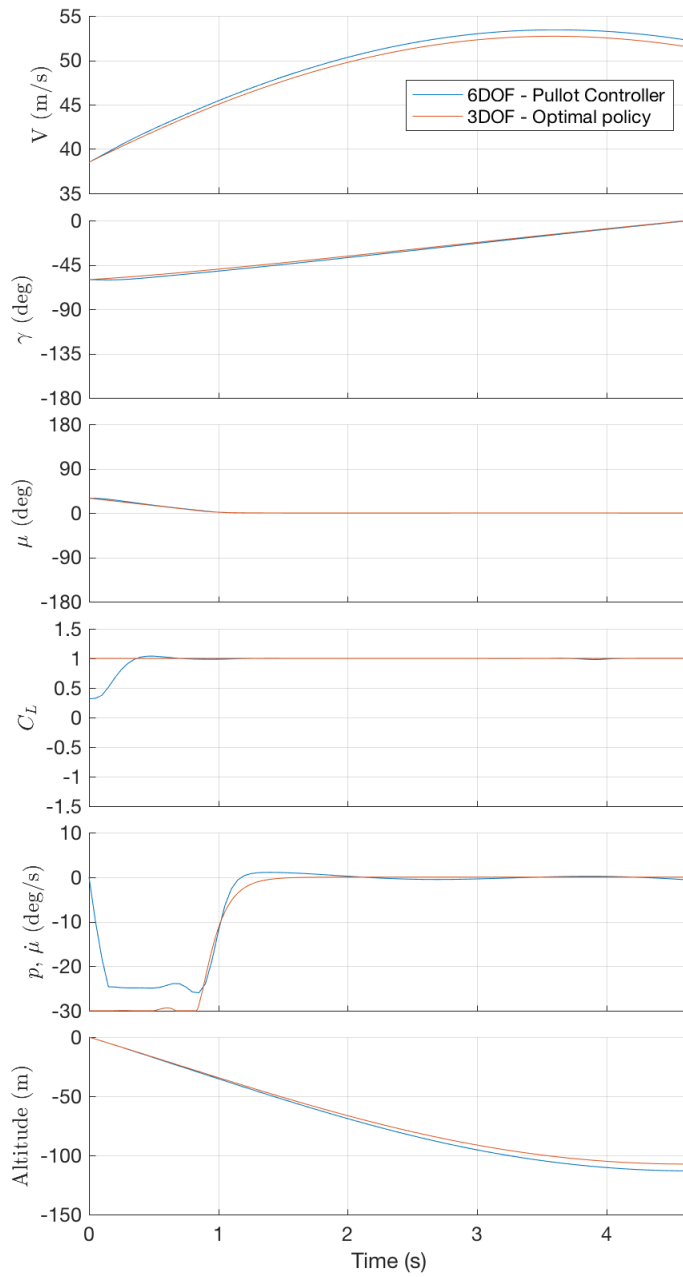
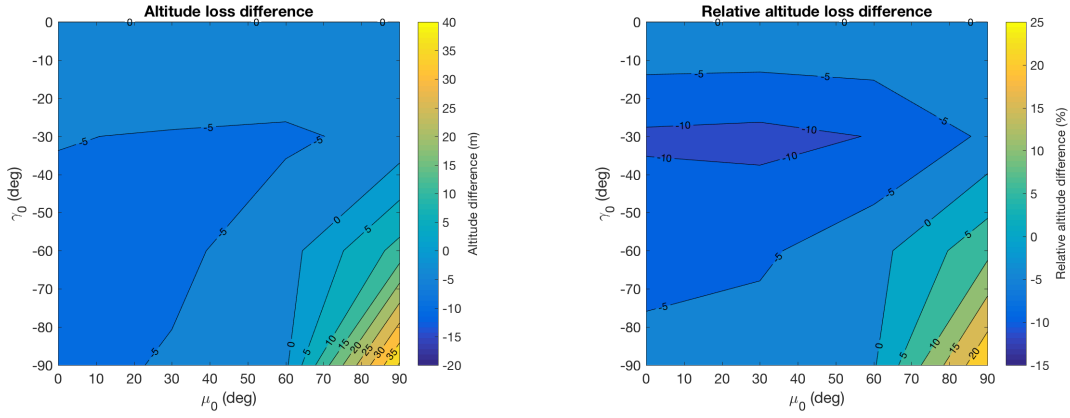


Figure 10. Example pullout maneuver on 6 and 3 DOF dynamic models.



(a) Altitude loss difference (altitude difference =  $h_{6DOF} - h_{3DOF}$ , where  $h$  is the altitude loss).  
 (b) Relative altitude loss difference (relative altitude difference =  $\frac{h_{6DOF} - h_{3DOF}}{h_{6DOF}}$ ).

**Figure 11. Altitude loss difference between the 6 DOF model with the proposed pullout controller and the 3 DOF model with the optimal policy.**

## VII. Conclusions and Future Work

Pullout maneuvers involve returning an initially diving aircraft to level flight. Aside from aerobatics, pullouts are usually the consequence of upsets, such as stall/spins. If these occur at low altitude, minimizing altitude loss becomes critical to avoid collision with the ground. This paper investigates the minimum altitude loss pullout maneuver, by first showing that the optimal control problem can be cast as an infinite horizon dynamic problem with an absorbing state at level flight. Following this, the optimal pullout policy is computed for a low-wing general aviation aircraft, using value iteration on a discretized reduced order point mass model of the aircraft dynamics, with lift coefficient and bank rate as control inputs. Results show a “bang-bang” type optimal policy whereby the lift coefficient and bank rate are maximized at each point, sometimes going from one extreme to the other upon crossing a set of switching surfaces. As expected, minimum altitude loss grows as the dive steepens and the bank angle increases, reaching as much as 200 meters for steep banked dives. Given that for this aircraft the stall lift coefficient for positive angles of attack is larger than for negative angles of attack, for most initial conditions the optimal action is to roll back to an upright attitude and effect a positive lift pullout. There is a region of the state-space though for which it is actually better to roll over and effect an inverted pullout. The effect of maximum lift coefficient on altitude loss is investigated, and results show that minimum altitude is very sensitive to this parameter, with an increase of approximately 20 meters for every tenth of dimensionless lift decreased. Corollary, increasing maximum lift coefficient decreases minimum altitude loss, indicating the potential benefit of using power and flaps during pullouts.

Having computed the optimal policy on a reduced order model, a pullout feedback controller is proposed, consisting of the optimal policy acting as an outer loop issuing lift coefficient and roll rate commands, and two inner loops adjusting elevator and aileron to track these commands. The roll rate controller consists of a simple proportional feedback loop achieving a rapid response. For the lift coefficient controller, a proportional gain on error plus pure damping from the pitch rate and a feedforward term provide a fast response with minimal overshoot allowing targeting high lift coefficients while ensuring no secondary stalls. The effectiveness of the controller is tested on 6 DOF simulations, showing that the altitude loss is indeed very close to the minimum altitude loss predicted by the reduce order model.

In doing the comparison between the 6 DOF and 3 DOF models, a deficiency in the 3 DOF model used to compute the optimal policy was observed for steep banked dives. Future work should investigate the effect of including an extra term to the bank rate equation of the reduced order model, which might explain the altitude loss discrepancy. Additionally, the effect of power, flaps, and the inclusion of higher order dynamics, like pitch and roll rate, in the optimal policy computation should be investigated, with a potential for further reduction of the minimum altitude loss.

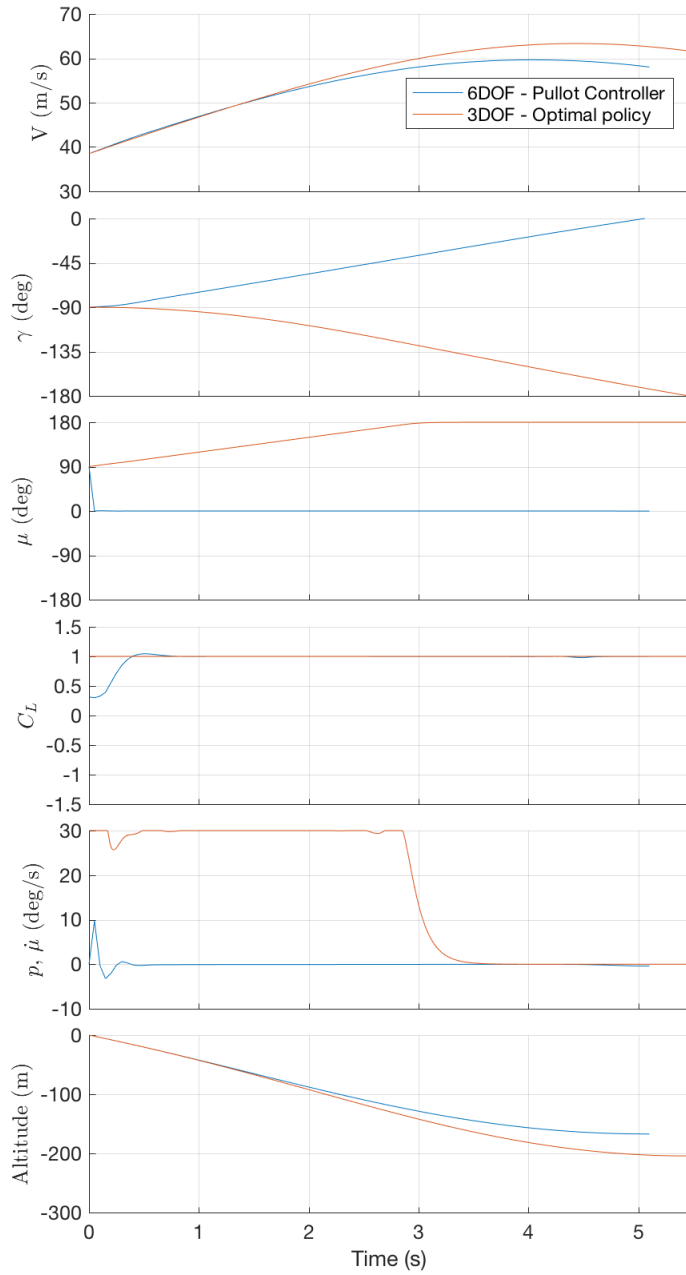


Figure 12. Pullout maneuver simulation for the 90 degree banked vertical dive.

## References

- <sup>1</sup>Stough, H. I., Patton, J. M. J., and Sliwa, S. M., “Flight Investigation of the Effect of Tail Configuration on Stall, Spin and Recovery Characteristics of a Low-Wing General Aviation Research Airplane (NASA-TP-2644),” NASA Langley Research Center, Hampton, VA, 1987.
- <sup>2</sup>Bunge, R. A., *Automatic Spin Detection and Recovery for Small Aircraft*, Ph.D. thesis, Stanford University, Stanford, CA, 2017.
- <sup>3</sup>Lanchester, F., *Aerodnetics: constituting the second volume of a complete work on aerial flight*, Bradbury, Agnew & Co. Ld., London, 1908.
- <sup>4</sup>Jones, R. T., “Dynamics of Ultralight Aircraft - Dive Recovery of Hang Gliders (NASA-TM-X-73229),” NASA Ames Research Center, Moffet Field, CA, 1977.
- <sup>5</sup>Vinh, N. X., *Optimal Trajectories in Atmospheric Flight*, Studies in Astronautics Vol. 2, Elsevier Scientific Pub. Co., 1981.
- <sup>6</sup>Schultz, R. L., “Three-Dimensional Trajectory Optimization for Aircraft,” *Journal of Guidance, Control, and Dynamics*, Vol. 13, No. 6, 1990, pp. 936–943.
- <sup>7</sup>Garcia, G., Keshmiri, S., and Huang, W., “Recovery of an Aircraft from the Loss of Control Using Open Final Time Dynamic Optimization and Receding Horizon Control,” *AIAA Guidance, Navigation, and Control Conference*, No. AIAA 2015-1545, Kissimmee, FL, 2015, pp. 1–9.
- <sup>8</sup>Bertsekas, D. P., *Dynammic Programming and Optimal Control*, Vol. 1, Athena Scientific, Belmont, MA, 3rd ed., 2005.
- <sup>9</sup>Newsom, W. A., Satran, D. R., and Johnson, J. L., “Effects of wing leading edge modifications on a low-wing full scale general aviation airplane: Wind Tunnel Investigation of High-Angle-of-Attack Aerodynamic Characteristics (NASA-TP-2011),” NASA Langley Research Center, Hampton, VA, 1982.
- <sup>10</sup>Ananda, G. K. and Selig, M. S., “Stall/Post-Stall Modeling of the Longitudinal Characteristics of a General Aviation Aircraft,” *AIAA Atmospheric Flight Mechanics Conference*, No. AIAA 2016-3541, Washington, D.C., 2016.
- <sup>11</sup>Riley, D. R., “Simulator study of the stall departure characteristics of a light general aviation airplane with and without wing-leading edge modification (NASA-TM-86309),” NASA Langley Research Center, Hampton, VA, 1985.
- <sup>12</sup>Kirk, D. E., *Optimal Control Theory: An introduction*, Dover Books on Electrical Engineering, Dover Publications, 2004.
- <sup>13</sup>Stevens, B. L. and Lewis, F. L., *Aircraft Control and Simulation*, Wiley, 2nd ed., 2003.
- <sup>14</sup>Kalviste, J., “Spherical Mapping and Analysis of Aircraft Angles,” *Journal of Aircraft*, Vol. 24, No. 8, 1987, pp. 523–530.

## Appendix

### A. Equations of Motion

#### 1. Body Velocity Components and Quaternions Representation

$$\dot{u} = rv - qw - g \sin \theta + \frac{(L \sin \alpha - D \cos \alpha)}{m} \quad (11a)$$

$$\dot{v} = -ru + pw + g \sin \phi \cos \theta + Y/m \quad (11b)$$

$$\dot{w} = qu - pv + g \cos \phi \cos \theta - \frac{(L \cos \alpha + D \sin \alpha)}{m} \quad (11c)$$

$$\dot{p} = \frac{M_x}{I_{xx}} - qr \frac{(I_{zz} - I_{yy})}{I_{xx}} - \frac{I_s^P}{I_{xx}} \dot{\Omega} \quad (11d)$$

$$\dot{q} = \frac{M_y}{I_{yy}} + pr \frac{(I_{zz} - I_{xx})}{I_{yy}} - \frac{1}{2} \frac{(I_y^P + I_z^P)}{I_{yy}} r \Omega \quad (11e)$$

$$\dot{r} = \frac{M_z}{I_{zz}} - pq \frac{(I_{yy} - I_{xx})}{I_{zz}} + \frac{1}{2} \frac{(I_y^P + I_z^P)}{I_{zz}} q \Omega \quad (11f)$$

$$\dot{\epsilon}_0 = -1/2(p\epsilon_1 + q\epsilon_2 + r\epsilon_3) \quad (11g)$$

$$\dot{\epsilon}_1 = 1/2(p\epsilon_0 - q\epsilon_3 + r\epsilon_2) \quad (11h)$$

$$\dot{\epsilon}_2 = 1/2(p\epsilon_3 + q\epsilon_0 - r\epsilon_1) \quad (11i)$$

$$\dot{\epsilon}_3 = 1/2(-p\epsilon_2 + q\epsilon_1 + r\epsilon_0) \quad (11j)$$

$$\begin{aligned} \dot{p}_x &= u \cos \theta \cos \psi + v(-\cos \phi \sin \psi + \sin \phi \sin \theta \cos \psi) \\ &\quad + w(\sin \phi \sin \psi + \cos \phi \sin \theta \cos \psi) \end{aligned} \quad (11k)$$

$$\begin{aligned} \dot{p}_y &= u \cos \theta \sin \psi + v(\cos \phi \cos \psi + \sin \phi \sin \theta \sin \psi) \\ &\quad + w(-\sin \phi \cos \psi + \cos \phi \sin \theta \sin \psi) \end{aligned} \quad (11l)$$

$$\dot{h} = u \sin \theta - v \sin \phi \cos \theta - w \cos \phi \cos \theta \quad (11m)$$

Where Euler angles  $\phi$ ,  $\theta$ ,  $\psi$  are a function of the quaternions as described in Ref. 13.

## 2. Flight Path and Flow Angles Representation

$$\dot{V} = -g \sin \gamma - \frac{(D \cos \beta - Y \sin \beta)}{m} \quad (12a)$$

$$\dot{\gamma} = \frac{L}{mV} \cos \mu - \frac{g}{V} \cos \gamma - \frac{(D \sin \beta + Y \cos \beta)}{mV} \sin \mu \quad (12b)$$

$$\dot{\xi} = \frac{L}{mV} \frac{\sin \mu}{\cos \gamma} + \frac{(D \sin \beta + Y \cos \beta) \cos \mu}{mV \cos \gamma} \quad (12c)$$

$$\begin{aligned} \dot{\mu} = & (\cos \beta + \tan \beta \sin \beta)(p \cos \alpha + r \sin \alpha) + (\sin \mu \tan \gamma + \tan \beta) \frac{L}{mV} \\ & + \frac{(D \sin \beta + Y \cos \beta)}{mV} \cos \mu \tan \gamma - \frac{g}{V} \cos \gamma \cos \mu \tan \beta \end{aligned} \quad (12d)$$

$$\dot{\alpha} = q - \sec \beta \left( \frac{L}{mV} - \frac{g}{V} \cos \gamma \cos \mu \right) - \tan \beta (p \cos \alpha + r \sin \alpha) \quad (12e)$$

$$\dot{\beta} = \frac{(D \sin \beta + Y \cos \beta)}{mV} + \frac{g}{V} \cos \gamma \sin \mu - (r \cos \alpha - p \sin \alpha) \quad (12f)$$

$$\dot{p} = \frac{M_x}{I_{xx}} - qr \frac{(I_{zz} - I_{yy})}{I_{xx}} - \frac{I_s^P}{I_{xx}} \dot{\Omega} \quad (12g)$$

$$\dot{q} = \frac{M_y}{I_{yy}} + pr \frac{(I_{zz} - I_{xx})}{I_{yy}} - \frac{1}{2} \frac{(I_y^P + I_z^P)}{I_{yy}} r \Omega \quad (12h)$$

$$\dot{r} = \frac{M_z}{I_{zz}} - pq \frac{(I_{yy} - I_{xx})}{I_{zz}} + \frac{1}{2} \frac{(I_y^P + I_z^P)}{I_{zz}} q \Omega \quad (12i)$$

$$\dot{h} = V \sin \gamma \quad (12j)$$

$$\dot{p}_x = V \cos \gamma \cos \xi \quad (12k)$$

$$\dot{p}_y = V \cos \gamma \sin \xi \quad (12l)$$

## 3. Flight Path and Euler Angles Representation

$$\dot{V} = -g \sin \gamma - \frac{(D \cos \beta - Y \sin \beta)}{m} \quad (13a)$$

$$\dot{\gamma} = \frac{L}{mV} \cos \mu - \frac{g}{V} \cos \gamma - \frac{(D \sin \beta + Y \cos \beta)}{mV} \sin \mu \quad (13b)$$

$$\dot{\xi} = \frac{L}{mV} \frac{\sin \mu}{\cos \gamma} + \frac{(D \sin \beta + Y \cos \beta) \cos \mu}{mV \cos \gamma} \quad (13c)$$

$$\dot{p} = \frac{M_x}{I_{xx}} - qr \frac{(I_{zz} - I_{yy})}{I_{xx}} - \frac{I_s^P}{I_{xx}} \dot{\Omega} \quad (13d)$$

$$\dot{q} = \frac{M_y}{I_{yy}} + pr \frac{(I_{zz} - I_{xx})}{I_{yy}} - \frac{1}{2} \frac{(I_y^P + I_z^P)}{I_{yy}} r \Omega \quad (13e)$$

$$\dot{r} = \frac{M_z}{I_{zz}} - pq \frac{(I_{yy} - I_{xx})}{I_{zz}} + \frac{1}{2} \frac{(I_y^P + I_z^P)}{I_{zz}} q \Omega \quad (13f)$$

$$\dot{\phi} = p + (q \sin \phi + r \cos \phi) \tan \theta \quad (13g)$$

$$\dot{\theta} = q \cos \phi - r \sin \phi \quad (13h)$$

$$\dot{h} = V \sin \gamma \quad (13i)$$

$$\dot{\psi} = \frac{(q \sin \phi + r \cos \phi)}{\cos \theta} \quad (13j)$$

$$\dot{p}_x = V \cos \gamma \cos \xi \quad (13k)$$

$$\dot{p}_y = V \cos \gamma \sin \xi \quad (13l)$$

Where the bank angle  $\mu$  is a function of  $(\theta, \psi, \phi, \gamma, \xi)$ , and can be calculated by first computing  $(\alpha, \beta)$  from  $(\theta, \psi, \phi, \gamma, \xi)$ , and from  $(\alpha, \beta, \theta, \psi, \phi)$  computing  $\mu$  (see Ref. 14 for more details).

## B. Aerodynamic Model for the Grumman American AA-1 Yankee

In this paper, a stability and control derivative model, as shown in Equation 14, is used. The coefficients are shown in Table 2, most of which were obtained from the aerodynamic tables published in<sup>11</sup> for an angle of attack of 5 deg, except for  $C_{l_{\delta a}}$  and  $C_{n_{\delta r}}$  which were not deemed correct, and instead were calculated from wind tunnel data published in.<sup>9</sup>

$$C_L = C_{L_0} + C_{L_\alpha} \alpha + C_{L_{\delta e}} \delta e + C_{L_q} \hat{q} \quad (14a)$$

$$C_D = C_{D_0} + C_{D_\alpha} \alpha + C_{D_{\alpha^2}} \alpha^2 \quad (14b)$$

$$C_m = C_{m_0} + C_{m_\alpha} \alpha + C_{m_{\delta e}} \delta e + C_{m_q} \hat{q} \quad (14c)$$

$$C_Y = C_{Y_\beta} \beta + C_{Y_p} \hat{p} + C_{Y_r} \hat{r} + C_{Y_{\delta a}} \delta a + C_{Y_{\delta r}} \delta r \quad (14d)$$

$$C_l = C_{l_\beta} \beta + C_{l_p} \hat{p} + C_{l_r} \hat{r} + C_{l_{\delta a}} \delta a + C_{l_{\delta r}} \delta r \quad (14e)$$

$$C_n = C_{n_\beta} \beta + C_{n_p} \hat{p} + C_{n_r} \hat{r} + C_{n_{\delta a}} \delta a + C_{n_{\delta r}} \delta r \quad (14f)$$

|       | $C_0$  | $\alpha$ | $\alpha^2$ | $\hat{q}$ | $\delta e$ | $\beta$ | $\hat{p}$ | $\hat{r}$ | $\delta a$ | $\delta r$ |
|-------|--------|----------|------------|-----------|------------|---------|-----------|-----------|------------|------------|
| $C_L$ | 0.4100 | 4.6983   | -          | 2.4200    | 0.3610     | -       | -         | -         | -          | -          |
| $C_D$ | 0.0525 | 0.2068   | 1.8712     | -         | -          | -       | -         | -         | -          | -          |
| $C_m$ | 0.0760 | -0.8938  | -          | -7.1500   | -1.0313    | -       | -         | -         | -          | -          |
| $C_Y$ | -      | -        | -          | -         | -          | -0.6303 | 0.0160    | 1.1000    | -0.0057    | 0.1690     |
| $C_l$ | -      | -        | -          | -         | -          | -0.1089 | -0.5200   | 0.1900    | -0.1031    | 0.0143     |
| $C_n$ | -      | -        | -          | -         | -          | 0.1003  | -0.0600   | -0.2000   | 0.0017     | -0.0802    |

Table 2. Stability and control derivatives for the AA-1X. All angular derivatives per radian.